International Journal of Nanomedicine

Dovepress
open access to scientific and medical research

Open Access Full Text Article

ORIGINAL RESEARCH

Bio-functionalized dense-silica nanoparticles for MR/NIRF imaging of CD146 in gastric cancer

This article was published in the following Dove Press journal:
International Journal of Nanomedicine
20 January 2015
Number of times this article has been viewed

Pu Wang[1,*]
Yazhuo Qu[2,*]
Chuan Li[3]
Li Yin[2]
Caifei Shen[1]
Wei Chen[3]
Shiming Yang[4]
Xiuwu Bian[2]
Dianchun Fang[1]

[1]Institute of Gastroenterology, [2]Institute of Pathology, [3]Department of Radiology, Southwest Hospital, The Third Military Medical University, Chongqing, People's Republic of China; [4]Department of Gastroenterology, Xinqiao Hospital, The Third Military Medical University, Chongqing, People's Republic of China

*These authors contributed equally to this work

Purpose: Nano dense-silica (dSiO$_2$) has many advantages such as adjustable core–shell structure, multiple drug delivery, and controllable release behavior. Improving the gastric tumor-specific targeting efficiency based on the development of various strategies is crucial for anti-cancer drug delivery systems.

Methods: Superparamagnetic iron oxide nanoparticles (SPION) were coated with dSiO$_2$ as core–shell nanoparticles, and labeled with near infra-red fluorescence (NIRF) dye 800ZW (excitation wavelength: 778 nm/emission wavelength: 806 nm) and anti-CD146 monoclonal antibody YY146 for magnetic resonance (MR)/NIRF imaging study in xenograft gastric cancer model. The morphology and the size of pre- and postlabeling SPION@dSiO$_2$ core–shell nanoparticles were characterized using transmission electron microscopy. Iron content in SPION@dSiO$_2$ nanoparticles was measured by inductively coupled plasma optical emission spectrometry. Fluorescence microscopy and fluorescence-activated cell sorter studies were carried out to confirm the binding specificity of YY146 and 800ZW–SPION@dSiO$_2$–YY146 on MKN45 cells. In vivo and in vitro NIRF imaging, control (nanoparticles only) and blocking studies, and histology were executed on MKN45 tumor-bearing nude mice to estimate the affinity of 800ZW–SPION@dSiO$_2$–YY146 to target tumor CD146.

Results: 800ZW–SPION@dSiO$_2$–YY146 nanoparticles were uniformly spherical in shape and dispersed evenly in a cell culture medium. The diameter of the nanoparticle was 20–30 nm with 15 nm SPION core and ~10 nm SiO$_2$ shell, and the final concentration was 1.7 nmol/mL. Transverse relaxivity of SPION@dSiO$_2$ dispersed in water was measured to be 110.57 $mM^{-1}\cdot s^{-1}$. Fluorescence activated cell sorter analysis of the nanoparticles in MKN45 cells showed 14-fold binding of 800ZW–SPION@dSiO$_2$–YY146 more than the control group 800ZW–SPION@dSiO$_2$. Series of NIRF imaging post intravenous injection of 800ZW–SPION@dSiO$_2$–YY146 demonstrated that the MKN45 xenograft tumor model could be clearly identified as early as a time point of 30 minutes postinjection. Quantitative analysis revealed that the tumor uptake peaked at 24 hours postinjection.

Conclusion: This is the first successful study of functional nanoparticles for MR/NIRF imaging of cell surface glycoprotein CD146 in gastric cancer model. Our results suggest that 800ZW–SPION@dSiO$_2$–YY146 nanoparticles will be applicable in tumor for image-guided therapy/surgery.

Keywords: SPION, nanotechnology, EMT, SPION@dSiO$_2$, xenograft, gastric cancer

Introduction

Cancer nanotechnology is an interdisciplinary area of research in life science with broad applications for treatment monitoring, early diagnosis, and targeted therapy. Nanotechnology offers an important novel tool to detect and modulate a variety of biomedical processes in vivo.[1] But the use of nanotechnology in gastric cancer (GC) is rarely reported; more than 930,000 patients are newly diagnosed with GC per year

Correspondence: Xiuwu Bian; Dianchun Fang
Institute of Gastroenterology, Southwest Hospital, The Third Military Medical University, Chongqing, People's Republic of China, 400038
Email bianxiuwu@263.net; fangdianchun@hotmail.com

worldwide and have many enigmatic traits, making it the fourth most common cancer.[2] Early detection and classification of GC are crucial for adopting appropriate treatment strategies. Due to the highly metastatic character of GC, the risk of relapse and resistance development after treatment is much higher for the first 3–5 years. A progressive subtype that causes severe prognosis can be worse even after patients undergo surgery and chemotherapy. Therefore, there is an urgent need for more specific and sensitive biomarkers to allow for accurate patient stratification and effective monitoring of the therapeutic response in patients with GC.[3]

It has been reported that in patients diagnosed with late-stage GC, the disease is often accompanied by a higher chance of metastasis. The epithelial-to-mesenchymal transition (EMT) is recognized as one of the major routes by which cancerous cells gain metastatic potential, and it is significantly correlated with poor survival of cancer patient.[4] EMT is an essential process in fetal morphogenesis, but in cancer cells, it is an early sign of metastatic potential. Recent studies have indicated that cell surface protein CD146 acts as a unique marker of EMT induction in cancer cells.[5] CD146, also known as MCAM, Mel-CAM, MUC18, or S-endo1, was first identified as a marker of tumor progression and metastasis in malignant melanomas.[6] The overexpression of CD146 correlates with cancer progression, EMT induction, invasion, and metastasis in a variety of malignancies. Due to its differential expression in metastases and advanced primary tumors, as well as its low background levels in normal tissue, CD146 has attracted considerable interest as a promising target for early diagnosis, prognosis, and therapy of cancer.

While the tumor burden and malignant progression are directly correlated with increased levels of CD146 expression, the location of abnormal expression of CD146 in aggressive cancer cells affords new tools for distinguishing cancer cells in the clinic.[7] The primary goal of this research is the early diagnosis of GC-related EMT by engineered nanoparticle molecular imaging. CD146 is found to be overexpressed in most of the gastric or gastroesophageal tumors, and in 50%–70% of esophageal cancers, it has been extensively used as a useful marker to evaluate the stage of GC.[8] Herein, we describe a novel marker CD146 on GC. YY146 is a mouse-anti-human monoclonal antibody (mAb) directed against CD146, a unique marker for EMT in the tumor metastasis.[9]

Superparamagnetic iron oxide nanoparticles (SPION) have outstanding features of biocompatibility, biodegradability, and low cost, making them one of the best candidate materials for the improvement of theranostics. However, the progress is limited.[10] An efficient drug vehicle must have three characteristics: moderate blood circulation time, great target accumulation rate, and high diffusion rate.[11] Traditional nano dense-silica (dSiO$_2$) nanoparticles and SPION are impeded by a roughly big size (>50 nm) and in vivo aggregation, which will make them susceptible to acute hepatic accumulation and poor extravasation rates.[12] More precisely, the surface of SPION is insensitive on drug loading, as opposed to the more popular drug carriers – carbon nanotubes. Till now, covalent linking is the preferred approach for most drug carriers. In this report, we produced SPION coated with dSiO$_2$ and labeled with 800ZW. They were easily functionalized with antibody in a very similar way as loading. 800ZW–SPION@dSiO$_2$–YY146 was injected via the tail vein to target MKN45 xenograft mouse model. Magnetic resonance (MR)/near infra-red fluorescence (NIRF) imaging was performed and the tumor tissue histology was evaluated to examine the pharmacokinetics of nanoparticles and to evaluate their unique role as in vivo marker for GC. As a result, with the evidence for CD146 as a novel marker for tumor metastasis, our work can provide new avenues for therapeutic interventions for the diagnosis and treatment of GC.

Methods

Reagents

SPION 15 nm was obtained from Ocean NanoTech (Springdale, AR, USA). Cy3-labeled and AlexaFluor488 secondary antibodies were from Jackson ImmunoResearch Laboratories, Inc. (West Grove, PA, USA); Alexa Fluor 647 secondary antibody and 4′,6-diamidino-2-phenylindole (DAPI) were from Invitrogen (Carlsbad, CA, USA). IRDye 800ZW-NHSester was obtained from LI-COR Biosciences Co. (Lincoln, NE, USA), and PD-10 desalting columns were from GE Healthcare (Piscataway, NJ, USA). All other chemicals used in this study were purchased from Sigma–Aldrich (St Louis, MO, USA).

Cell culture and animal model

MKN45 cells were purchased from the American Type Culture Collection (ATCC; Manassas, VA, USA). All cells were cultured at 37°C in 5% CO_2 atmosphere in appropriate tissue culture medium and passaged for no longer than 2 months. Cells were used for experiments (in vitro and in vivo) when they reached ~80% confluence.

In our study, MKN45 cells were used to generate xenograft tumor model on nude mice. All the animal studies were conducted in compliance with the guidance for the care and use of laboratory animals and were approved by the Life Science Research Ethics Committee of the Institute

of Southwest Hospital, Third Military Medical University (Chongqing, People's Republic of China). Nude mice were obtained from the Southwest Hospital Animal Center of the Third Military Medical University. For the animal tumor models, 6- to 8-week-old female nude mice were selected, and tumors were established by subcutaneous injection of 1×10^6 MKN45 cells resuspended in 100 µL of 1:1 mixture of Dulbecco's Modified Eagle's Medium and Matrigel (BD Biosciences, Franklin Lakes, NJ, USA) into the rear flank of mice. The tumor sizes were monitored every 2 days, and the animals were subjected to in vivo experiments when the size of tumors was over 5 mm (about 15 days after inoculation).

Synthesis of 800ZW–SPION@dSiO$_2$–YY146

Figure 1 shows the four major steps in the synthesis of 800ZW–SPION@dSiO$_2$–YY146.[13,14] SPION coated with uniform dSiO$_2$ nanoparticles were functionalized first with –NH$_2$ groups by (3-aminopropyl) trimethoxysilane to form SPION@dSiO$_2$–NH$_2$ (1), followed by polyethylene glycolylation (PEGylation) with SCM-PEG5k-maleimide (MAD) to achieve SPION@dSiO$_2$–PEG–Mal, leaving amino (succinimidyl carboxymethyl ester [SCM]) groups on the shell for further antibody conjugations. Afterward, the desired number of 800ZW (2) were added to obtain 800ZW–SPION@dSiO$_2$–PEG-Mal (3) Lastly, polyethylene glycol (PEG) (Mal-PEG5k-SCM) was used to acquire 800ZW–SPION@dSiO$_2$–YY146 (4), which was reacted with YY146-SH.

Characterization of the nanoparticles

The morphology and the size of pre- and post-labeling SPION@dSiO$_2$ core–shell nanoparticles were characterized using transmission electron microscopy (TEM), FEI T12, with an accelerating voltage of 120 kV. Samples were diluted and dropped on to a carbon-coated copper grid. Iron content in SPION@dSiO$_2$ nanoparticle dispersion was measured by Inductively Coupled Plasma Optical Emission Spectrometry. T2 relaxation time was measured using a multi-slice multi-echo sequence. Transverse (r_2) relaxivity in the unit of per millimolar per second was calculated through curve fitting of the reciprocal of the T2 relaxation time versus the iron concentration (mM Fe).[13] The characterization of the prepared nanoparticles on the particle size and zeta potential was determined by dynamic light scattering (DLS) spectrophotometer, and zeta potential analysis was performed on Nano-Zetasizer (Malvern Instruments, Malvern, UK). The nanoparticles were centrifuged and resuspended in phosphate-buffered saline (PBS) prior to the experiment. The size and zeta potential of the nanoparticles were determined using the manufacturer's instructions.

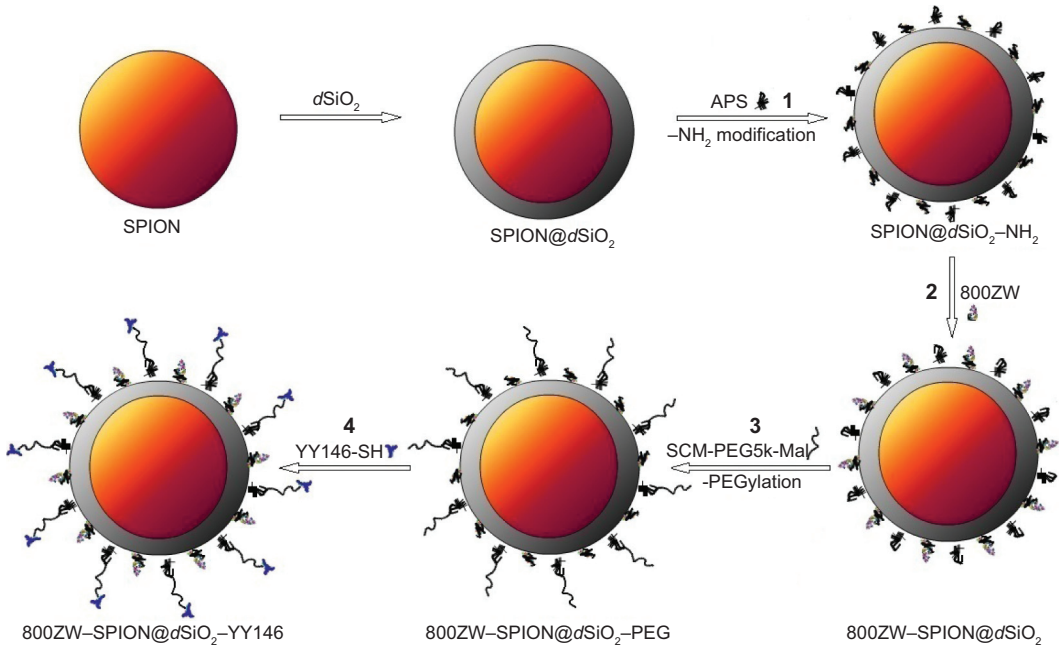

Figure 1 A schematic illustration of the synthesis of 800ZW–SPION@dSiO$_2$–YY146.

Notes: Uniform dSiO$_2$-coated SPION nanoparticles (**1**) were first modified with –NH$_2$ groups to form dSiO$_2$NH$_2$. (**2**) dSiO$_2$–NH$_2$ was labeled with 800ZW for NIRF imaging and subsequent –NH$_2$ to PEG; (**3**) afterward, PEGylated with SCM-PEG5k-Mal to form 800ZW–SPION@dSiO$_2$–PEG; (**4**) which was then subjected to mAb conjugation to form 800ZW–SPION@dSiO$_2$–YY146.

Abbreviations: SPION, superparamagnetic iron oxide nanoparticles; NIRF, near infra-red fluorescence; PEG, polyethylene glycol; mAb, monoclonal antibody; APS, ammonium persulfate.

Determination of binding affinities of CD146

The binding affinities of the immunoreactivity of 800ZW–SPION@*d*SiO_2–YY146 to MKN45 (high CD146 expression) were detected by fluorescence activated cell sorter (FACS) technique. Briefly, adherent and suspended MKN45 cells were harvested and dissociated into single-cell suspension in PBS with 2% bovine serum albumin at the concentration of 5×10^5 cells/mL for FACS studies. Samples were incubated with 70 µL of 5 nmol/mL 800ZW–SPION@*d*SiO_2–YY146, 70 µL of 5 nmol/mL 800ZW–SPION@*d*SiO_2, blocking with 200 µg ×3 of YY146, and 70 µL of 5 nmol/mL 800ZW–SPION@*d*SiO_2–YY146 for 30 minutes at 37°C. The cells were washed three times with PBS, centrifuged at 1,500 rpm for 4 minutes, and then incubated with 7-aminoactinomycin for 1 minute at 37°C. After that, the stained cells were cleaned and analyzed using BD FACS Calibur equipped with 633 nm channel (Becton Dickinson, San Jose, CA, USA) and FlowJo 7.0 analysis software (Tree Star, Inc., Ashland, OR, USA).

Immunofluorescence staining and confocal microscopy images

Cells were also incubated with 800ZW–SPION@*d*SiO_2–YY146 (5 nmol/mL) and then observed under a Leica microscope to further confirm the results from FACS. Cells were cultured at a density of 0.5×10^4 cells/well on 10×10 mm cover slip in 24-well plate and cultured for 24 hours, then the cells were washed three times with PBS and fixed in 4% paraformaldehyde in PBS. Later, they were permeabilized with 0.1% Triton X-100 and blocked with 1% bovine serum albumin in PBS. Primary antibodies used were anti-albumin (1:500; Sigma-Aldrich) and YY146 (1:500). Secondary antibodies were mouse anti-human Alexa Fluor 647. The cells were counterstained with DAPI.

MR/NIRF imaging

For imaging studies, 800ZW–SPION@*d*SiO_2–YY146 was concentrated and injected into the tail vein at an amount of 200 µL per mouse. Isoflurane was kept at 2% in O_2 for the status of anesthesia. T2-weighted images were obtained on a magnetic resonance imaging (MRI) system (Siemens, Erlangen, Germany), before and at 4, 24, and 48 hours after the tail vein injection. The mice were imaged at the same time points after injection in a Kodak scanner using the ICG and X-ray channels. Signal intensities were measured by defined regions-of-interests (ROIs) with Image J software (NIH, Bethesda, MD, USA). To confirm the CD146 specificity of 800ZW–SPION@*d*SiO_2–YY146 in vivo, three mice were each pre-injected with 200 µg ×3 of YY146 before administration (ie, blocking) of 800ZW–SPION@*d*SiO_2–YY146. After scanning, mice were euthanized. Blood, tumor tissue, and major organs/tissues were collected and imaged ex vivo to affirm the findings in vivo. Using the analysis software, ROIs on the MKN45 tumors were labeled and compared with other organs of ROIs. The average signal intensity within the ROI (in the unit of counts per second per square millimeter) was used for further data analysis. The final fluorescence intensity of the MKN45 tumor was presented as mean ± SD (n=3).

Histology

Frozen tissue slices of 5 µm thickness were fixed with 3% ice acetone for 15 minutes and dried for 20 seconds naturally in the air. After PBS cleaning and blocking with 10% donkey serum at room temperature for 30 minutes, the nuclei were stained with DAPI, and then the confocal microscopic images of the slices were obtained using a TCSSP5 laser-scanning confocal microscope (Leica). All the figures were produced using 40× and oil-immersion objective. Images were quantified and analyzed using LAS AF Lite software (Leica).

Statistical analysis

Quantitative data were expressed as the mean ± SD and the means compared by Student's *t*-test, *P*-values <0.05 were considered significant.

Results

Characterization of 800ZW–SPION@*d*SiO_2–YY146

800ZW–SPION@*d*SiO_2–YY146 nanoparticles with an average size of 50 nm were prepared by following the procedures mentioned above. Figure 2 shows the representative TEM figure of prepared SPION@*d*SiO_2 and 800ZW–SPION@*d*SiO_2–YY146 with spheroidal structures. The size of SPION@*d*SiO_2 could easily be regulated simply by changing the size of SPION. SPION@*d*SiO_2 and 800ZW–SPION@*d*SiO_2–YY146 show a typical core–shell structure. No obvious morphological changes of 800ZW–SPION@*d*SiO_2–YY146 were observed after shell modifications, as evidenced by TEM data in Figure 2.

The successful surface modifications were validated by zeta potential measurements and DLS, the diameters of 800ZW–SPION@*d*SiO_2–YY146 nanoparticles based on DLS became larger after the surface modifications, such as the amination layer, PEG chains, and YY146. The final product of 800ZW–SPION@*d*SiO_2–YY146 could

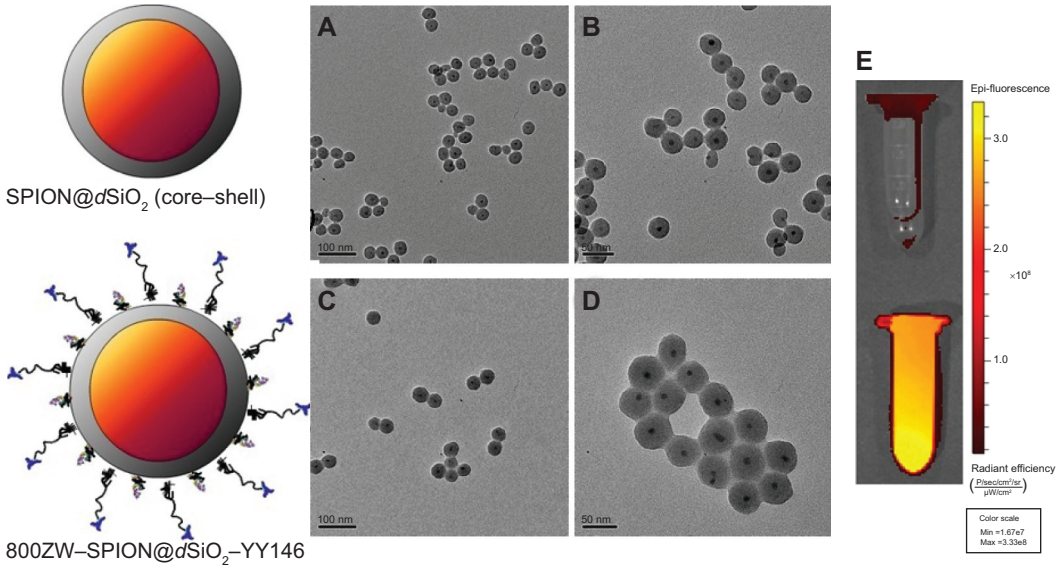

Figure 2 Schematic and TEM/NIRF pictures of actual structures before and after surface modification.
Notes: (**A**) A TEM image of SPION@dSiO$_2$ (core–shell) before surface modification (scale bar =100 nm). (**B**) A zoomed-in TEM image of SPION@dSiO$_2$ (core–shell) before surface modification (scale bar =50 nm). (**C**) A TEM image of 800ZW–SPION@dSiO$_2$–YY146 (scale bar =100 nm). (**D**) A magnified TEM image of 800ZW–SPION@dSiO$_2$–YY146 (scale bar =50 nm). (**E**) An NIRF imaging of nanoparticle (upper) of SPION@dSiO$_2$ and (down) 800ZW–SPION@dSiO$_2$–YY146 in PBS solution.
Abbreviations: TEM, transmission electron microscopy; SPION, superparamagnetic iron oxide nanoparticles; NIRF, near infra-red fluorescence; PBS, phosphate-buffered saline; Min, minimum; Max, maximum.

be redispersed in PBS solution easily and no obvious aggregation was observed in a couple of weeks. The surface modification and DLS diameter of 800ZW–SPION@dSiO$_2$–YY146 were found to be 146±5 nm and 3.6±3.2 mV, respectively. Taken together, these results confirmed the successful functional modifications of SPION@dSiO$_2$ nanoparticles into the 800ZW–SPION@dSiO$_2$–YY146 nanoconjugates.

T2 relaxivity coefficient of SPION@dSiO$_2$

After ten times dilution of SPION@dSiO$_2$ and dispersion of the nanoparticles in deionized water, the Fe concentration obtained by inductively coupled plasma optical emission spectrometry was 21.9 ppm, 3.9 mmol/L. Then, the samples were diluted and observed in T2-weighted images (Figure 3A–D), from the graph, r_2 relaxivity was derived to be 110.57 mM^{-1}·s^{-1} (Figure 3E).

800ZW–SPION@dSiO$_2$–YY146 in vitro binding affinities of CD146

800ZW–SPION@dSiO$_2$ conjugated with YY146 did not alter its binding ability to MKN45, as proved by both FACS analysis (Figure 4) and confocal data (Figure 5). FACS analysis of MKN45 (which has a strong expression of YY146) showed 14-fold 800ZW–SPION@dSiO$_2$–YY146 than the control group 800ZW–SPION@dSiO$_2$. On treatment with 800ZW–SPION@dSiO$_2$ or 800ZW–SPION@dSiO$_2$–YY146 using the blocking dose of YY146 (200 μg each time, three in

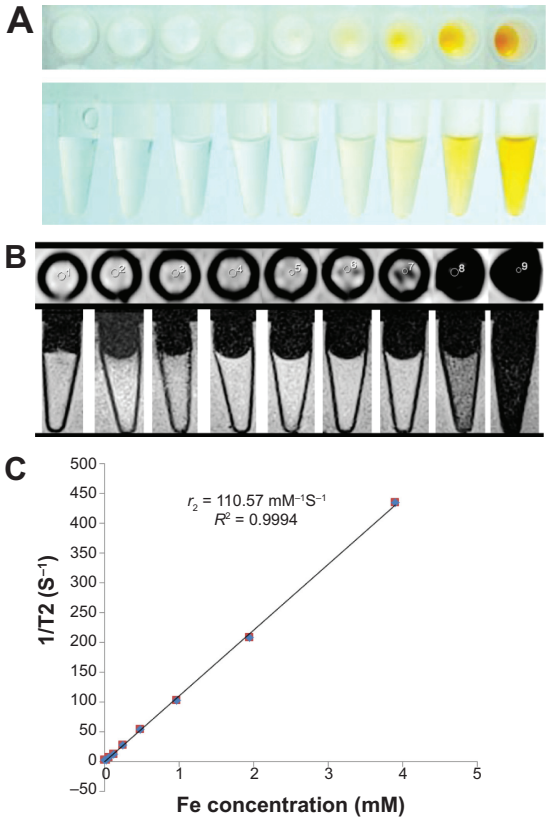

Figure 3 T2 relaxivity coefficient (r_2) stability test of SPION@dSiO$_2$.
Notes: (**A**) Photograph of SPION@dSiO$_2$ aqueous solutions with different Fe concentrations, from 0 to 3.9 mmol/L. T2-MR images of SPION@dSiO$_2$ (**B**) in deionized water, obtained by using a 3.0 T clinical MR imaging instrument. (**C**) Inverse transverse relaxation times (1/T2) versus Fe concentration. The slope indicates that the T2 relaxivity coefficient (r_2) =110.57 mM^{-1}·s^{-1}.
Abbreviations: SPION, superparamagnetic iron oxide nanoparticles; MR, magnetic resonance.

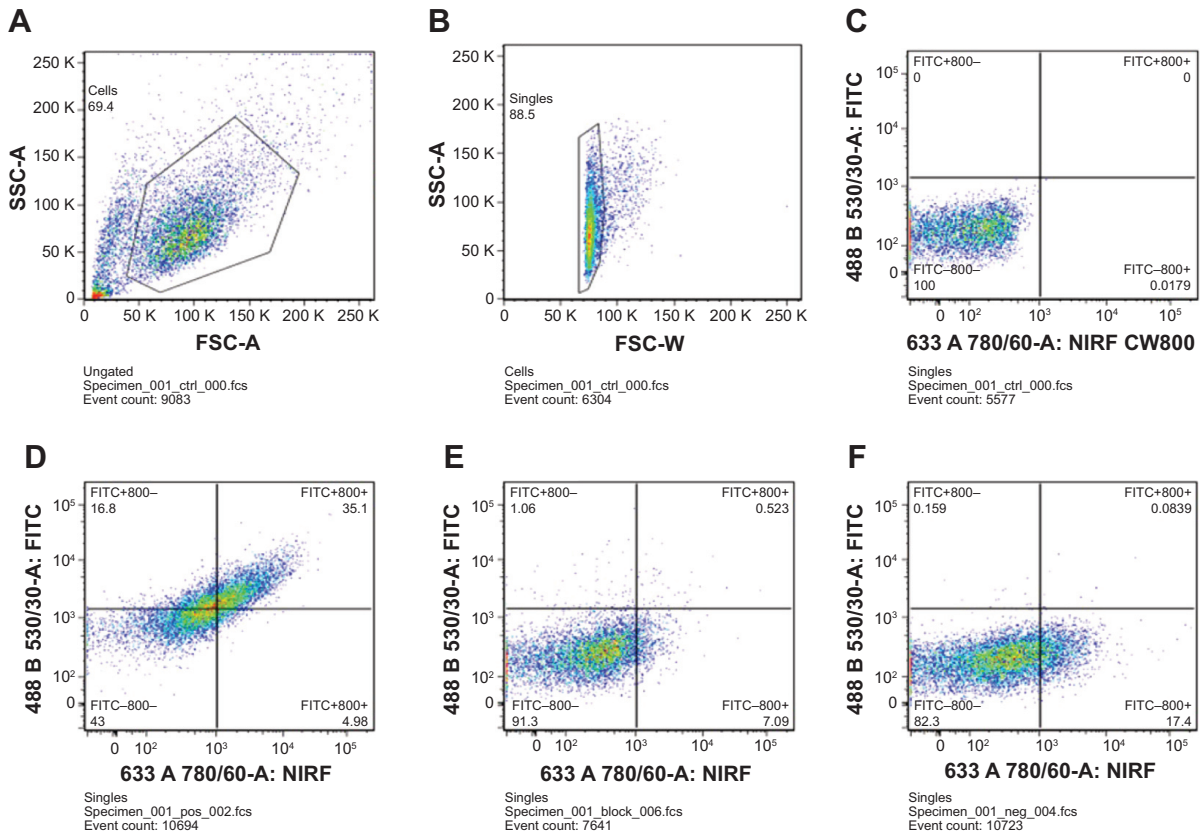

Figure 4 In vitro investigation of 800ZW–SPION@*d*SiO_2–YY146 conjugation.
Notes: FACS analysis of 800ZW–SPION@*d*SiO_2–YY146 conjugation in MKN45 (CD146 positive) cells after 30 minutes incubation and subsequent washing. (**A**) Whole cells FACS distribution; (**B**) analysis gate for the single cells. (**C**) Control group: cells are all located at the NIRF channel negative. (**D**) Target group: 40.08% cells are labeled by NIRF dye; (**E**) blocking group: the labeled cells drop to 7.532% after YY146 blocking; (**F**) negative group: 17.4839% labeling in the negative group.
Abbreviations: SPION, superparamagnetic iron oxide nanoparticles; FACS, fluorescence activated cell sorter; NIRF, near infra-red fluorescence; SSC, side scatter; FSC, forward angle light scatter; FITC, fluorescein isothiocyanate.

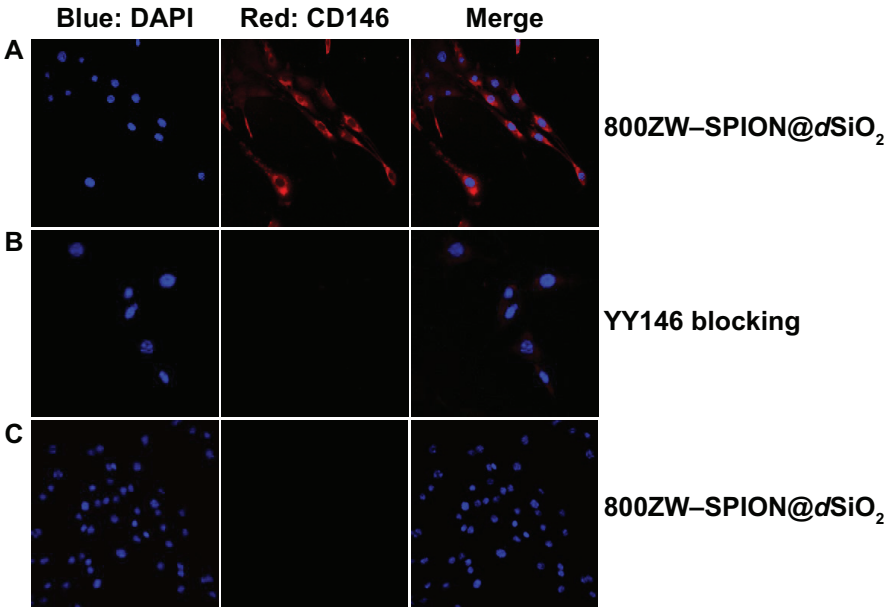

Figure 5 Confocal microscopic image of 800ZW–SPION@*d*SiO_2–YY146.
Notes: In vitro investigation of nanoparticle binding affinities of CD146 on MKN45 cells: cells were incubated with (**A**) 70 μL of 5 nmol/mL 800ZW–SPION@*d*SiO_2–YY146, targeting group (**B**) YY146 (200 μg ×3) blocking and 70 μL of 5 nmol/mL 800ZW–SPION@*d*SiO_2–YY146, (**C**) 70 μL of 5 nmol/mL 800ZW–SPION@*d*SiO_2. Strong staining of cell membrane was observed in targeting group (**A**) whereas background levels were seen in blocking (**B**) and control (**C**) (40× oil).
Abbreviations: SPION, superparamagnetic iron oxide nanoparticles; DAPI, 4′,6-diamidino-2-phenylindole.

total), only a slight fluorescence enhancement (0.15-fold and 1.0-fold, respectively) was observed. Taken together, these in vitro experiments confirmed that 800ZW–SPION@dSiO$_2$ conjugation did not impact the antigen-binding specificity of YY146.

In vivo MR/NIRF imaging about tumor targeting

The time points at 4, 16, 24, and 48 hours post 800ZW–SPION@dSiO$_2$–YY146 injection (pi) were chosen for a series of NIRF scanning. The coronal slices of MKN45 tumors are shown in Figure 6 and the Supplementary material (Figures S1–S3). Quantitative data obtained from ROIs analysis of the NIRF images are shown in Figure 7. In addition, representative MR images of MKN45 xenograft bearing mice at 4, 24, and 48 hours pi of 800ZW–SPION@dSiO$_2$–YY146 are shown in Figure 8 for direct visualization. Figure 8 shows T*2-weighted MR images collected at specific time points on the T system, where 800ZW–SPION@dSiO$_2$–YY146 appears as discontinued, intermittent, and negative contrast ROIs. A significant signal drop in image contrast occurred between the time points 24 and 48 hours followed by a continual decrease thenceforth. The observation of apparent distinction is peaked at 24 hours of 800ZW–SPION@dSiO$_2$–YY146 injection.

Prominent NIRF signals from the tumor liver, kidney, and spleen biodistribution indicated significant accumulation of 800ZW–SPION@dSiO$_2$–YY146 in the main organs at 48 hours pi (Figure 9 and Figure S4), which is consistent with the in vivo findings. The NIRF of 800ZW–SPION@dSiO$_2$–YY146 demonstrated weak overlap with CD31 staining of blood vessels, revealing that the uptake of 800ZW–SPION@dSiO$_2$–YY146 in the main organs was most likely owing to the nonspecific capture of phagocytes and/or other processes that are not relevant to the expression of CD146.

The liver uptake of three groups was found to be 426.18±12.15 (21%/g at 48 hours pi) and tumor uptake was 280.46±7.04 (intensity of fluorescence signal, 14.02%/g at 48 hours pi; n=3; Figure 7), as was expected from intravenously injected nanomaterials. Importantly, accumulation of 800ZW–SPION@dSiO$_2$–YY146 in the tumor happened fast, which can be visible clearly at 4 hours pi and peaked at around 24 hours pi, as shown in Figure 8. In comparison, in unconjugated nanoparticles, the MKN45 tumor uptake of 800ZW–SPION@dSiO$_2$ was found to be significantly lower than that of 800ZW–SPION@dSiO$_2$–YY146 at all

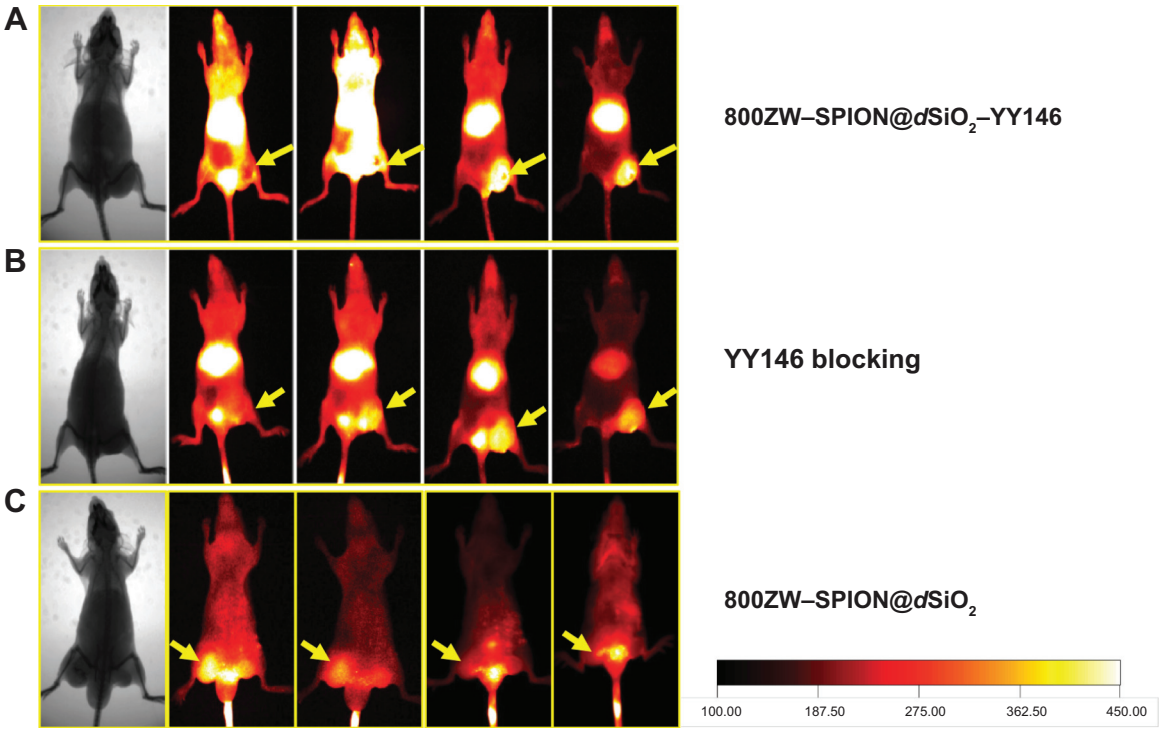

Figure 6 NIRF imaging.
Notes: Serial coronal NIRF images of MKN45 tumor-bearing mice at different time points postinjection of (**A**) 800ZW–SPION@dSiO$_2$–YY146, (**B**) 800ZW–SPI N@dSiO$_2$ with a blocking dose of YY146, or (**C**) 800ZW–SPION@dSiO$_2$. Tumors are indicated by yellow arrowheads.
Abbreviations: NIRF, near infra-red fluorescence; SPION, superparamagnetic iron oxide nanoparticles.

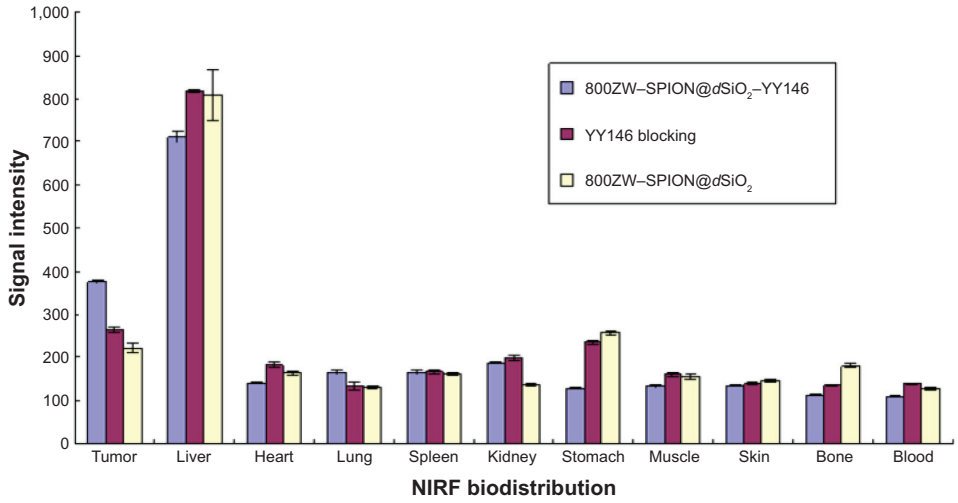

Figure 7 Biodistribution analysis.
Notes: The MKN45 tumor uptake of 800ZW–SPION@dSiO$_2$ after 48 hours pi was found to be significantly lower than that of 800ZW–SPION@dSiO$_2$–YY146 at those time points examined, indicating that YY146 conjugation was the controlling factor for enhanced tumor uptake of 800ZW–SPION@dSiO$_2$–YY146 ($P<0.05$).
Abbreviations: SPION, superparamagnetic iron oxide nanoparticles; pi, postinjection; NIRF, near infra-red fluorescence.

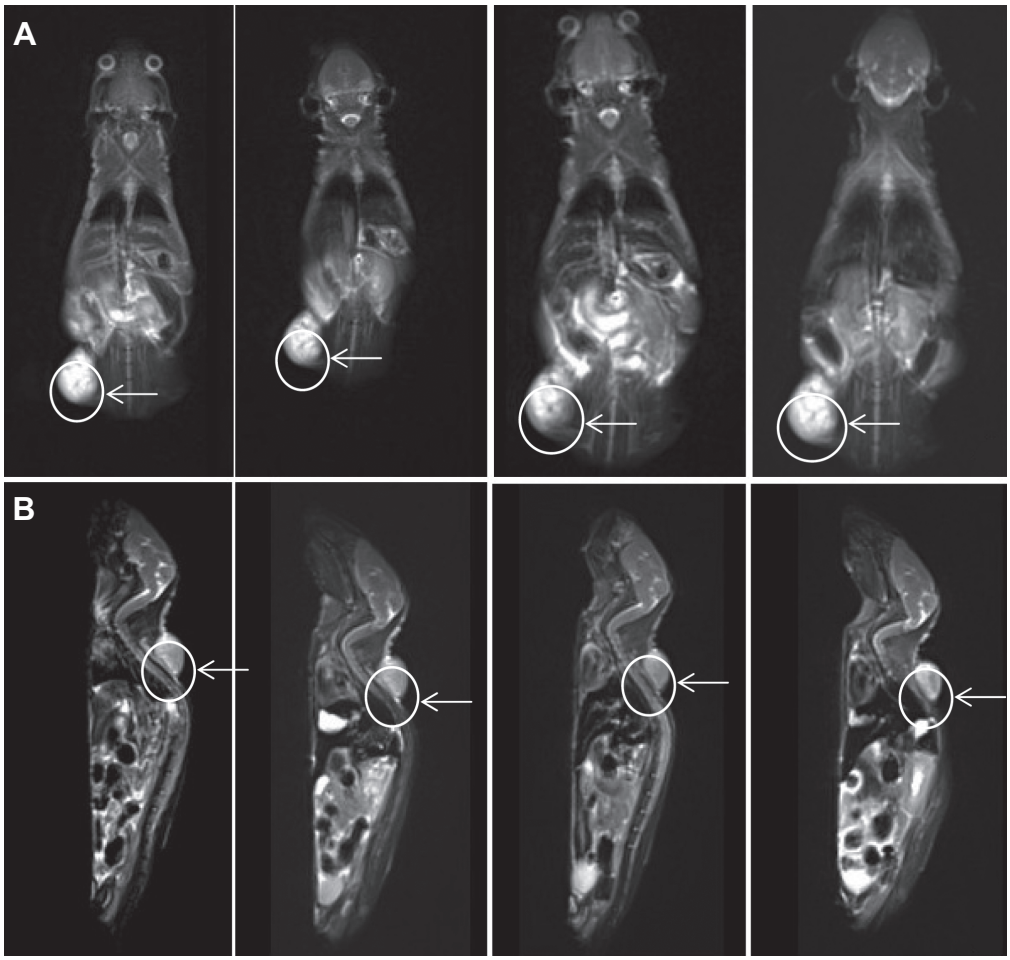

Figure 8 MR imaging.
Notes: A series of pictures showed T2-weighted MR images acquired at the defined time points on the 11.7 T system, where (**A**) 800ZW–SPION@dSiO$_2$–YY146 appeared as discrete, punctuated, negative contrast regions. A significant decrease in image contrast occurred between the time points 24 and 48 hours followed by a gradual decrease thereafter; (**B**) 800ZW–SPION@dSiO$_2$, as the image arrows were shown, it was difficult to find the change among prescanning and three time points. Tumors are indicated by white arrows.
Abbreviations: MR, magnetic resonance; SPION, superparamagnetic iron oxide nanoparticles.

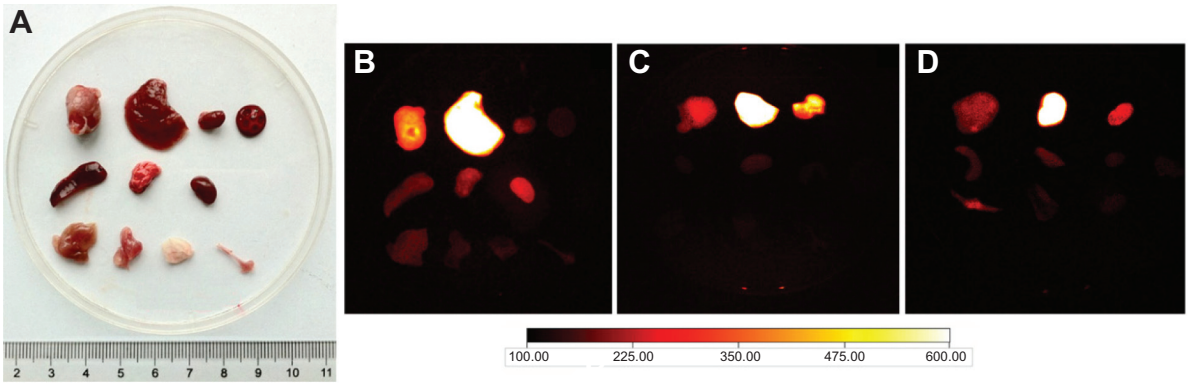

Figure 9 Ex vivo imaging of the three groups.
Notes: Prominent NIRF signal from the tumor, liver, kidney, and spleen biodistribution indicated significant uptake of (**A**) white light photograph, (**B**) 800ZW–SPION@*d*SiO_2–YY146, (**C**) 800ZW–SPION@*d*SiO_2 with a blocking dose of YY146, (**D**) 800ZW–SPION@*d*SiO_2 in these three organs at 48 hours pi, which corroborated the in vivo findings.
Abbreviations: NIRF, near infra-red fluorescence; SPION, superparamagnetic iron oxide nanoparticles; pi, postinjection.

time points examined, 121.59±7.84 (6.08%/g at 48 hours pi; n=3; Figure 7), indicating that YY146 conjugation was the key factor for the enhancement of tumor uptake of 800ZW–SPION@*d*SiO_2–YY146.

Histology studies

To confirm our understanding about the nanoparticle distribution in the organs and tissues, we carried out a series of immune staining. Notably, these nanoparticles exhibited a non-uniform distribution across the tumor, observed from the MRI. A separate study supported our observation, where tumor slices were stained with DAPI and imaged with confocal microscopy directly. Immunofluorescence CD146 staining of MKN45 cells and CD146/CD31 staining of xenograft tumor tissues revealed that CD146 was highly expressed in the MKN45 tumor (Figure 10). The ex vivo assessment of the tumor tissues found weak consistency between the particles. It should be mentioned that, owing to the limited resolution, nothing but spots with particle accumulation can be observed by confocal microscopy. Therefore, signals from the uptake in the liver and spleen were mostly irrelevant to CD146 affinity and more roughly connected with the nonspecific uptake by the reticuloendothelial system.

Discussion

Successful surface modification of *d*SiO_2 is the first crucial step for obtaining shell coating, in vivo stability, and efficient tumor targeting imaging/drug delivery. The surface amination of *d*SiO_2 is critical for the following surface modifications, which were effectively done by reacting (3-aminopropyl) trimethoxysilane with *d*SiO_2 in absolute ethanol at 90°C. In this study, surface PEGylation was carried out to enhance YY146 conjugation, to ensure that the nanoparticles are steady in the physiological environment, and to decrease the phagocytosis by the immune system to improve the lifetime of blood circulation of 800ZW–SPION@*d*SiO_2–YY146 in mice. The characterization of 800ZW–SPION@*d*SiO_2–YY146 (eg, zeta potential, TEM, and DLS) affirmed the success of nanoparticle conjugation,

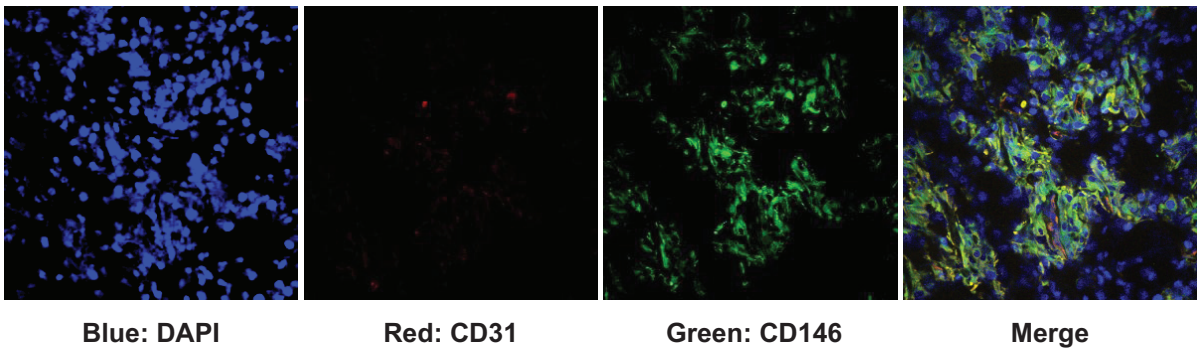

Figure 10 Immunofluorescence staining of MKN45 tumor tissue.
Notes: CD146/CD31 staining of xenograft tumor tissues revealed that CD146 was highly expressed on the MKN45 tumor (40× oil). Green: CD146; red: CD31; blue: DAPI.
Abbreviation: DAPI, 4′,6-diamidino-2-phenylindole.

and the product could be well redispersed in PBS without obvious accumulation for weeks.

Abnormal protein expression is usually bilateral and involves complex networks of signal pathways. In this study, we introduced biofunctionalized *d*SiO_2 as a multiple carrier for early diagnosis and target treatment for GC. CD146 was previously proposed as a potential melanoma marker that was responsible for tumor recurrence based on different EMT pathways. We investigated the in vitro effects of YY146 on GC cells because CD146 can be a good target in vivo. MR/NIRF imaging technique was adopted here as a powerful tool in the screening of mAb due to its high sensitivity in the detection of molecular changes in multiple diseases prior to the development of clinical symptoms. FACS showed good cell binding with 800ZW–SPION@*d*SiO_2–YY146. As expected, histology revealed that tumor tissue had strong and uniform distribution of CD146 signal. In some previous studies, CD146 was confirmed to induce EMT in many tumor cells.[15] Recent novel molecular advances in EMT have contributed to a better understanding of EMT pathophysiology and disease stratification. This observation indicates that CD146 can induce tumor cells to undergo EMT and transfer some cells into a more aggressive state during tumor progression. YY146 can be very useful in tumor spotting, metastasis detection, and treatment response monitoring. The studies will help elucidate the roles of novel therapeutic EMT signaling pathways and factors in cancer. They will provide important new mechanistic insights into how anti-CD146 mAb-based molecular imaging can help early diagnosis of GC and enhance patient stratification. Better understanding of its role may facilitate patient selection and lead to treatment optimization. Our long-term objective is to develop versatile contrast agent-based pharmaceutics for both molecular imaging and therapy of GC.

Later, we tried dual-modality YY146 on GC to monitor the targeting by imaging techniques. 800ZW–SPION@*d*SiO_2–YY146 have the potential to be widely used in biomedicine, such as in multiple service platforms in MRI. There have been several successful attempts reporting MRI contrast agent modification, such as multiple imaging motifs. Another aim is to ship drugs by using nanosystems to achieve a multifunctional theranostic mediator that integrates diverse capacities, such as imaging diagnosis, drug loading, and therapeutic monitoring. Multifunctional SPION@*d*SiO_2 nanoplatform offers a great potential in the foreseeable era of personal theranostics by providing specific treatment and monitoring. Traditional MRI contrast agent-SPION limits the theranostics progress due to their drawbacks of particle size (>50 nm) and magnetic aggregation, making them weakly resistant to hepatic accumulation and lacking in extravasation rates. We also used a dual-modality labeling system to doubly monitor the antibody-based imaging. YY146 showed a strong positive GC accumulation. The results show that 800ZW–SPION@*d*SiO_2–YY146 targeted GC in vivo by binding to EMT marker CD146 on tumor cells. Most importantly, we also demonstrated the feasibility of using 800ZW–SPION@*d*SiO_2–YY146 for noninvasive monitoring of early tumor responses to anti-metastasis therapies, showing higher sensitivity than common approaches based on measurements of tumor size.

Furthermore, the target/non-target tumor ratios are strong enough to confirm an obvious tumor targeting. All in vivo imaging data validated the feasibility of GC imaging by targeting CD146. It is noteworthy that, after dual-modality, YY146 still illustrated high tumor/muscle ratio, primary GC can be detected specifically. However, patients with more aggressive metastatic tumors will get little to no benefit in overall survival as the responses are often altered. Moreover, latest reports have showed that multiple levels of inhibitors or gene inactivation lead to the enhancement of tumor invasiveness in a series of preclinical animal models of tumor.

The stability of the dual-modality nanoparticle and the surface labeling are the most important concerns of this study, which can cause false-positive results. However, FACS examination in vitro demonstrated that the surface label detachment was not strong enough to affect the targeting of the nanoparticles. The anti-CD146 mAb can be conjugated onto such a nanosystem without obvious alteration in the physical characterization of nanoparticles. It is remarkable for the formulation optimization, which differs for each particular drug loading because of numerous alterable factors (the basic character of particles, the efficiency of drug loading, and in vivo stability). It is worthwhile to point out that, an amine-rich coating layer of 800ZW–SPION@*d*SiO_2–YY146 can be occupied in part by binding sites of CD146, but it does not compromise the loading ability of the drug molecules. Furthermore, any favorable recipient can be incorporated into this nanosystem, such as peptides, proteins, and novel drug molecules.

Conclusion

We have successfully accomplished in vivo noninvasive monitoring of YY146 labeling with dual-modality biofunctionalized *d*SiO_2-coated SPION nanoparticles as MRI/NIRF

contrast agents in xenografted GC model in mice. The results show that 800ZW–SPION@*d*SiO_2–YY146 target GC in vivo by binding to a novel tumor marker of CD146. Undoubtedly, such results are important in the clinic to decrease the side effects and treatment costs, specifically with the increasing number of alternative treatments that are only effective in particular groups of patients.

Acknowledgments

This work was funded by a Strategic Priority Research Program of the Chinese Academy of Sciences (H1808-81201140 and H1608-81272442). The authors thank Professor Weibo Cai and Dr Feng Chen from the University of Wisconsin–Madison for technical assistance on nanoparticles synthesis and nanoparticles character analysis.

Disclosure

The authors declare no conflicts of interest in this work.

References

1. Sun D, Liu Y, Yu Q, et al. Inhibition of tumor growth and vasculature and fluorescence imaging using functionalized ruthenium-thiol protected selenium nanoparticles. *Biomaterials*. 2014;35(5):1572–1583.
2. Siegel R, Naishadham D, Jemal A. Cancer statistics, 2013. *CA Cancer J Clin*. 2013;63(1):11–30.
3. Sehdev A, Catenacci DV. Gastroesophageal cancer: focus on epidemiology, classification, and staging. *Discov Med*. 2013;16(87):103–111.
4. Cho JY. Molecular diagnosis for personalized target therapy in gastric cancer. *J Gastric Cancer*. 2013;13(3):129–135.
5. Koyama Y, Okayama H, Kumamoto K, et al. Overexpression of endoglin (CD105) is associated with recurrence in radically resected gastric cancer. *Exp Ther Med*. 2010;1(4):627–633.
6. Johnson JP, Lehmann JM, Stade BG, Rothbächer U, Sers C, Riethmüller G. Functional aspects of three molecules associated with metastasis development in human malignant melanoma. *Invasion Metastasis*. 1989;9(6):338–350.
7. Zhang W, He XJ, Ma YY, et al. Inducible nitric oxide synthase expression correlates with angiogenesis, lymphangiogenesis, and poor prognosis in gastric cancer patients. *Hum Pathol*. 2011;42(9):1275–1282.
8. Barzi A, Lenz HJ. Angiogenesis-related agents in esophageal cancer. *Expert Opin Biol Ther*. 2012;12(10):1335–1345.
9. Rosen LS, Hurwitz HI, Wong MK, et al. A phase I first-in-human study of TRC105 (Anti-Endoglin Antibody) in patients with advanced cancer. *Clin Cancer Res*. 2012;18(17):4820–4829.
10. Stamopoulos D, Manios E, Gogola V, et al. Bare and protein-conjugated Fe(3)O(4) ferromagnetic nanoparticles for utilization in magnetically assisted hemodialysis: biocompatibility with human blood cells. *Nanotechnology*. 2008;19(50):505101.
11. Zhang F, Huang X, Qian C, et al. Synergistic enhancement of iron oxide nanoparticle and gadolinium for dual-contrast MRI. *Biochem Biophys Res Commun*. 2012;425(4):886–891.
12. Chen F, Bu W, Chen Y, et al. A sub-50-nm monosized superparamagnetic Fe_3O_4@SiO_2 T2-weighted MRI contrast agent: highly reproducible synthesis of uniform single-loaded core-shell nanostructures. *Chem Asian J*. 2009;4(12):1809–1816.
13. Yi P, Chen G, Zhang H, et al. Magnetic resonance imaging of Fe_3O_4@SiO_2-labeled human mesenchymal stem cells in mice at 11.7 T. *Biomaterials*. 2013;34(12):3010–3019.
14. Chen F, Hong H, Zhang Y, et al. In vivo tumor targeting and image-guided drug delivery with antibody-conjugated, radiolabeled mesoporous silica nanoparticles. *ACS Nano*. 2013;7(10):9027–9039.
15. Kalluri R. EMT: when epithelial cells decide to become mesenchymal-like cells. *J Clin Invest*. 2009;119(6):1417–1419.

Supplementary material

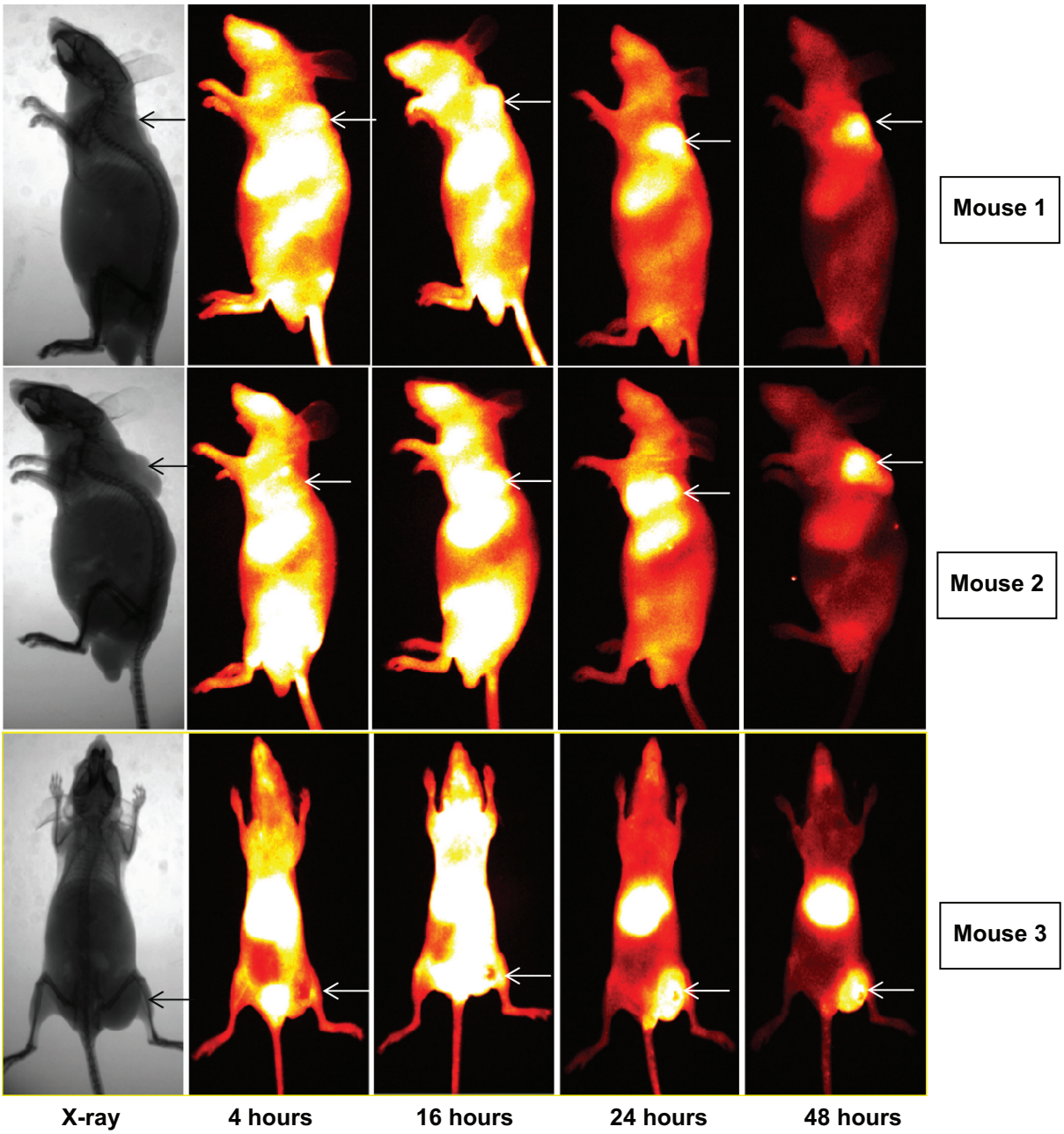

Figure S1 NIRF images of positive group, tumors are indicated by white arrows.
Abbreviation: NIRF, near infra-red fluorescence.

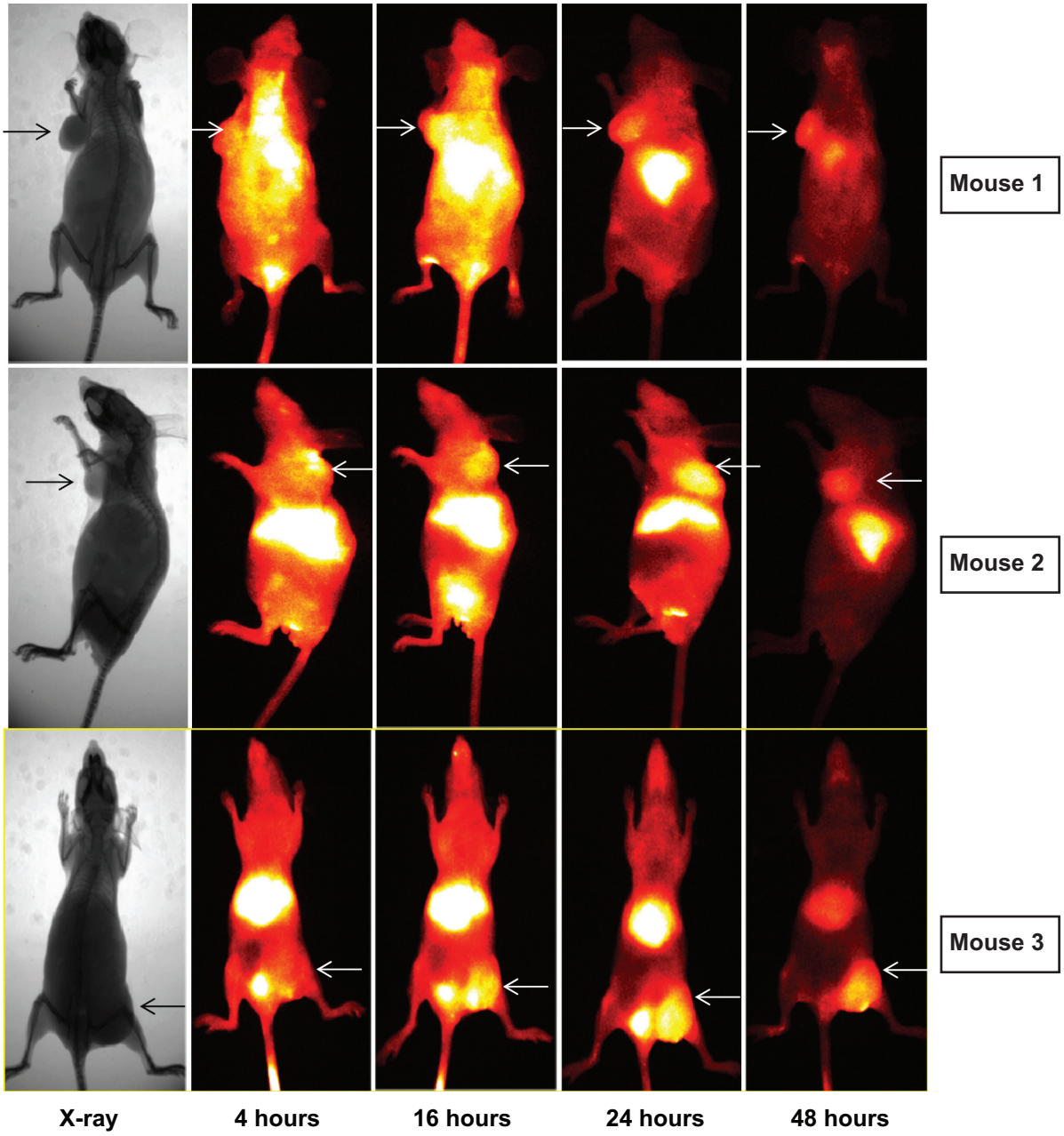

Figure S2 NIRF images of blocking group, tumors are indicated by white arrowheads.
Abbreviation: NIRF, near infra-red fluorescence.

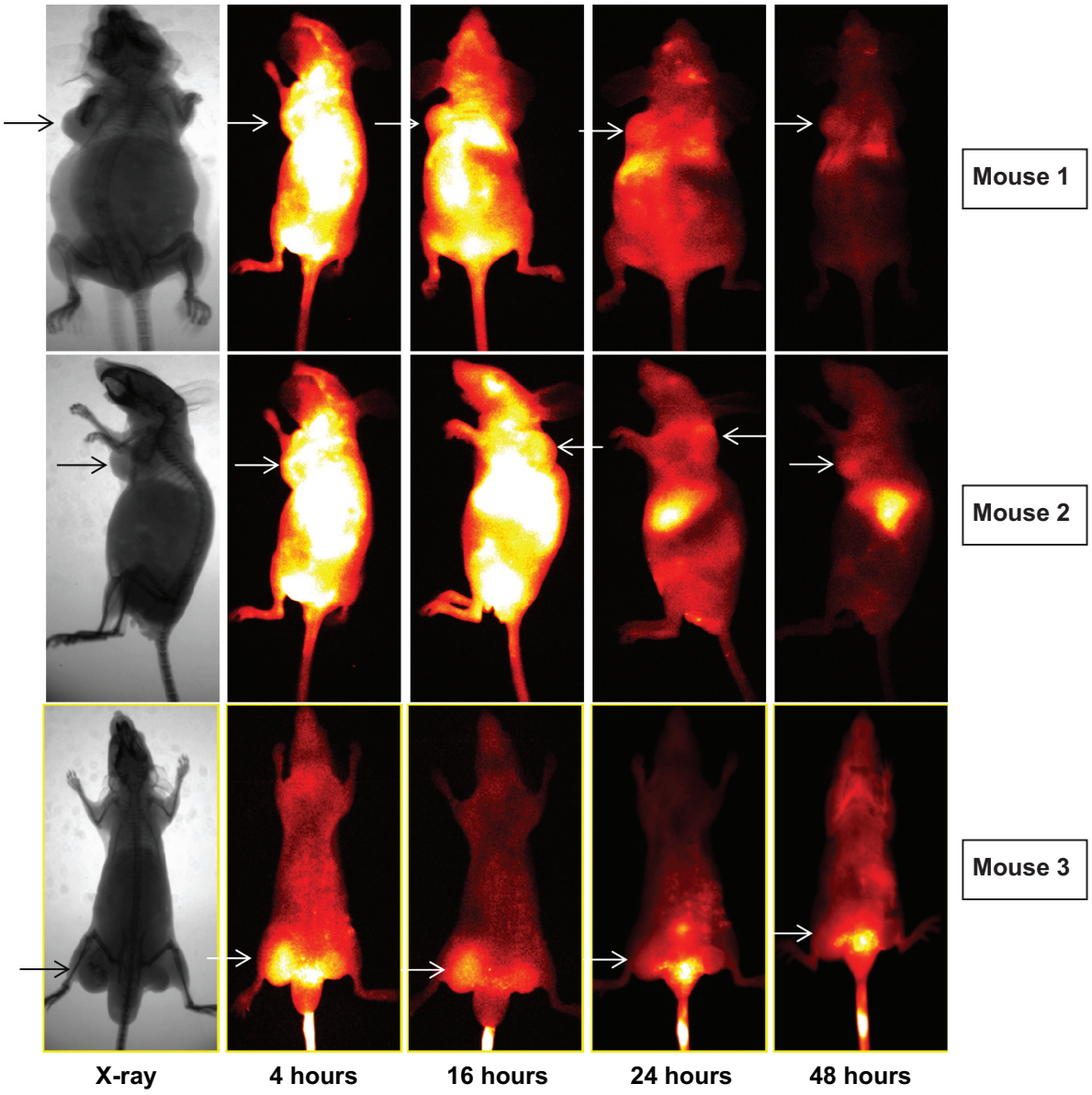

Figure S3 Biodistribution of blocking group, tumors are indicated by white arrowheads.

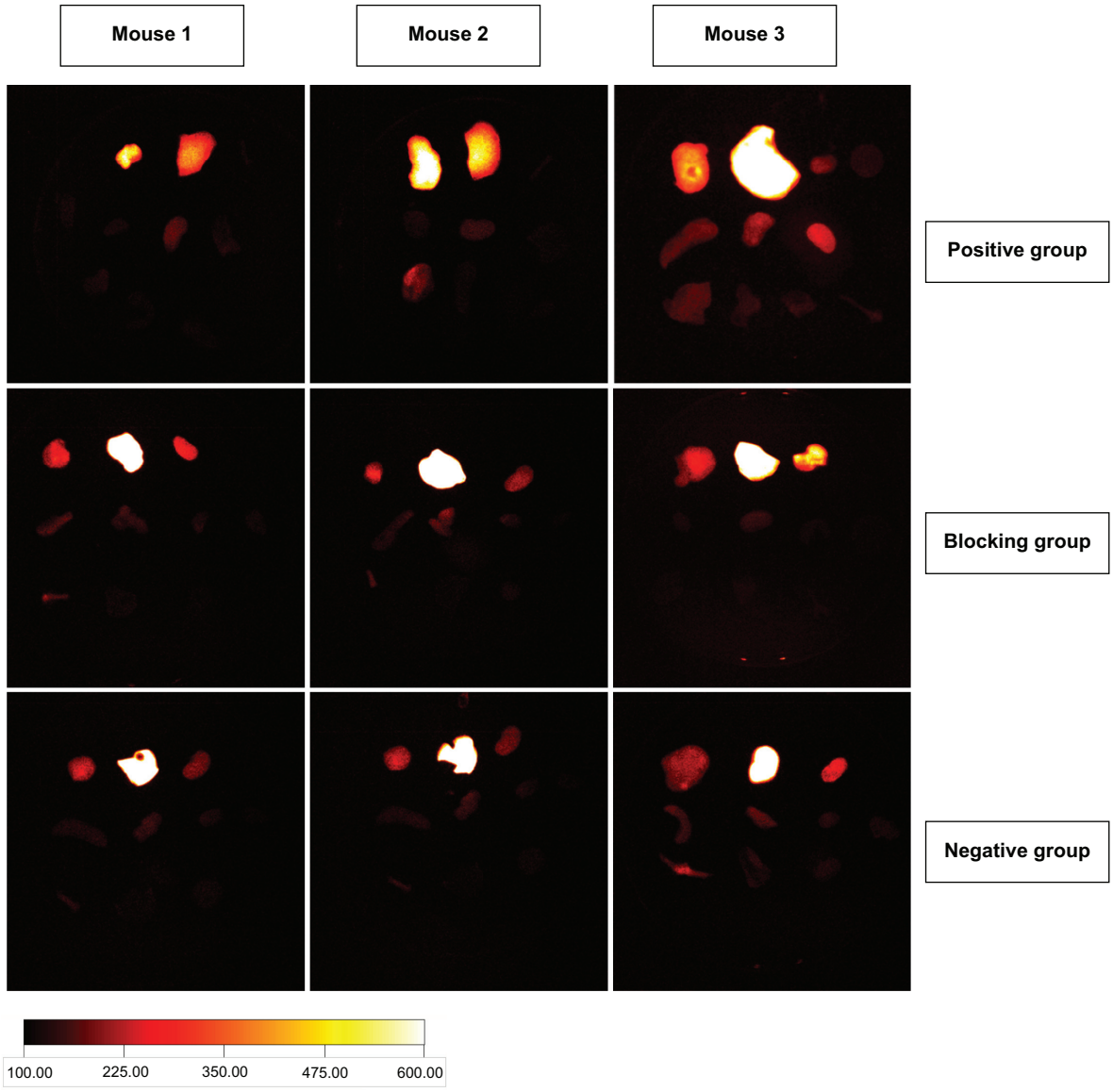

Figure S4 Biodistribution of three groups.